Check for updates

# Heterogeneous Fenton-like catalysis of Fe-MOF derived magnetic carbon nanocomposites for degradation of 4-nitrophenol†

Dezhi Chen, [ID] *[a] Shasha Chen,[a] Yijie Jiang,[a] Shasha Xie,[a] Hongying Quan,[b] Li Hua,[a] Xubiao Luo [ID] *[a] and Lin Guo[ac]

Magnetic carbon nanocomposites (Fe–$C_x$) as heterogeneous Fenton-like catalysts were synthesized by the pyrolysis of iron based metal-organic frameworks (Fe-MOF), and the degradation removal of 4-nitrophenol (4-NP) in aqueous solution was used to evaluate the catalytic activity of Fe–$C_x$. The results showed that 4-NP could be effectively degraded by Fe–$C_x$ in the presence of hydrogen peroxide. Pyrolysis temperature significantly affected the component, structures and performances of the catalysts, and the as-prepared Fe–$C_{500}$ exhibited the best catalytic performance. Furthermore, the effects of several reaction conditions, such as catalyst loading, $H_2O_2$ dosage, reaction temperature, and initial pH, on the catalytic degradation of 4-NP were extensively analyzed for the practical applications of Fe–$C_{500}$. At an initial circumneutral pH of 6.21, 89.0% of 0.36 mM 250 mL of 4-NP solution could be degradated after 75 min by the heterogeneous Fenton-like oxidation on the 0.08 g $L^{-1}$ of Fe–$C_{500}$ in the presence of 7.8 mM $H_2O_2$. The results of activation energy and the reaction kinetics showed Fe–$C_{500}$ possessed a high catalytic activity in the heterogeneous Fenton reaction of 4-NP. Moreover, the prepared Fe–$C_{500}$ could be reused by an external magnet, and still retained good catalytic activity with 52.4% degradation of 4-NP at the fourth cycle.

## 1. Introduction

With the wide use of pesticides, drugs, dyes, and other organic matter, increasingly detrimental pollutants are discharging into environment, which will cause great damage to the health of humans and other creatures.[1,2] Therefore, it is significant to take effective measures to dispose of these contaminants. Various methods, including adsorption,[3] flocculation,[4] membrane filtration,[5] microorganism degradation,[6] have been investigated and developed to remove organic pollutants from effluent. However, some of these processes suffer from drawbacks such as partial degradation of the effluent, toxic by-products and excessive sludge production, energy consumption, and secondary phase generation that imposes extra cost in the process.[7–9] Therefore, it is necessary to improve the

*[a]Key Laboratory of Jiangxi Province for Persistent Pollutants Control and Resources Recycle, School of Environmental and Chemical Engineering, Nanchang Hangkong University, No. 696, Fenghe South Avenue, Nanchang, 330063, China. E-mail: chendz@nchu.edu.cn; luoxubiao@nchu.edu.cn*

*[b]School of Materials Science and Engineering, Nanchang Hangkong University, No. 696, Fenghe South Avenue, Nanchang 330063, China*

*[c]Key Laboratory of Bio-Inspired Smart Interfacial Science and Technology of Ministry of Education, School of Chemistry and Environment, Beihang University, No. 37 Xueyuan Road, Haidian District, Beijing 100191, China*

† Electronic supplementary information (ESI) available. See DOI: 10.1039/c7ra09234b

treatment efficiency of conventional wastewater treatment methods. Advanced oxidation processes (AOPs), such as Fenton oxidation consisting of catalyst ($Fe^{2+}/Fe^{3+}$) and hydrogen peroxide ($H_2O_2$), have been found to be effective at degrading recalcitrant and chemically complicated organics contaminants.[10,11] However, there are still certain limitations regarding the application of Fenton oxidation processes. The homogeneous type operates in a narrow range of pH (2–4), and large quantities of acid are required and a neutralization step is required afterward.[11–15] Furthermore, the stoichiometric amounts of iron are required, and very hard to remove after the reaction. Therefore, this process can also generate secondary pollution (*e.g.* acid or metal ions) as well as metal hydroxide sludge. To overcome these problems, heterogeneous Fenton-like catalysts based on iron-containing solids have been intensively investigated.[13,14,16–21] Among iron-containing solids, magnetic recoverable nanoparticles ($Fe_3O_4$, $\gamma$-$Fe_2O_3$, and $Fe^0$) show effective heterogeneous Fenton catalyst because of their highly acceptable reusability and stability, low toxicity, and easy separation.[22–24] However, these magnetic iron-based nanoparticles have a strong tendency to agglomerate, resulting in the reduce of their catalytic activity.[25,26] To circumvent the obstacle, carbonaceous materials with high conduct electricity, specific surface area and porosity, have been widely chosen as matrices for loading of magnetic nanoparticles, which not only can enhance electron transfer and increase the active sites for the

degradation of pollutants in water but also facilitate the separation of catalyst from water system.[14,25,27–29]

Recently, the pyrolysis of metal–organic frameworks (MOFs) has been considered an effective and simple way to construct magnetic recoverable iron-containing nanoparticles/porous carbon composites using in Fenton-like reaction for the degradation of organic pollution in aqueous system.[17,30–32] For example, MIL-53(Fe)-derived magnetic $\gamma$-$Fe_2O_3$/C showed high catalytic activity for the degradation of malachite green under sunlight in the presence of $H_2O_2$.[30] Magnetic iron/carbon nanorods derived from MIL-88A could activate peroxide for the decolorization of rhodamine B in water.[17] During the pyrolysis process, these Fe-MOFs were gradually decomposed to magnetic iron-containing nanoparticles/porous carbon composites with the increase of temperature under inert atmosphere. Therefore, the pyrolysis temperature is key factor for the morphology, structure, and activity of product. However, until now there has been a lack of such information to the best of our knowledge. Herein, porous magnetic carbon composites with iron-based nanoparticles were prepared by the thermal decomposition of Fe-MOF at different temperature in $N_2$ atmosphere. The catalytic activity of obtained magnetic products for the heterogeneous Fenton-like degradation of 4-nitrophenol (4-NP) in aqueous solution was studied in detail.

## 2. Experimental section

### 2.1 Materials

Iron(III) chloride hexahydrate ($FeCl_3 \cdot 6H_2O$), $p$-phthalic acid (PTA), $N,N$-dimethylformamide (DMF), hydrogen peroxide ($H_2O_2$), ethanol, $n$-butyl alcohol was analytical reagent grade and used directly without further purification.

### 2.2 Preparation of Fe-MOF and magnetic carbon nanocomposites

Fe-MOF was synthesized by the previous report with some modifications.[33] In a typical preparation, 15.5 g $FeCl_3 \cdot 6H_2O$ and 10.6 g PTA was mixed in 640 mL DMF solution by magnetic stirring until complete dissolution, and then the above mixture was transferred into a three-neck round bottom flask connected to condenser and heated at 100 °C for 12 hours in an oil bath with magnetic stirring. After naturally cooled to room temperature, the supernatant was centrifuged to obtain orange-yellow product. The product was washed using ethanol for several times and dried in vacuum at 80 °C for 24 hours. Finally, the solid Fe-MOF powder was annealed in a tube furnace at different temperature (400 °C, 450 °C, 500 °C, 550 °C, 600 °C) (ramp rate, 1 °C min$^{-1}$) for 1 hour in a $N_2$ atmosphere to prepare the magnetic carbon nanocomposites. The obtained magnetic carbon materials were labelled as Fe–$C_x$, where $x$ denoted the heating temperature.

### 2.3 Characterization

Thermogravimetric analysis (TGA) was used to measure the thermal stability of the Fe-MOF. X-ray diffractometer (XRD, D8 Advanced, Bruker, at 40 kV and 40 mA, Cu K$\alpha$ radiation,

$\lambda = 1.5406$ Å) and scanning electron microscope (FEI Quanta 450) with an acceleration voltage of 10 kV was used to characterize the phase and morphology of Fe-MOF and magnetic Fe–$C_x$ nanocomposites, respectively. X-ray photoelectron spectroscopy (XPS, Thermo Scientific ESCALAB 250, A1 K$\alpha$ radiation) was used to analyse the elemental composition and corresponding chemical state in the surface of Fe-MOF and magnetic Fe–$C_x$ nanocomposites. TriStar II 3020 surface area and pore size analyser (Micromeritics) was used to obtain the nitrogen adsorption–desorption isotherms of magnetic Fe–$C_x$ nanocomposites. The specific surface area, total pore volume and pore-size distribution of the Fe–$C_x$ nanocomposites was determined by the Brunauer–Emmett–Teller (BET) and Barrett–Joyner–Halenda (BJH) method, respectively. Magnetic properties were tested using a physical properties measurement system (PPMS-DynaCool, Quantum Design, USA) equipped with a 9T vibrating sample magnetometer (VSM).

### 2.4 Heterogeneous Fenton-like catalytic activity measurement

The target contaminate was 4-nitrophenol (4-NP). In a typical experiment, 250 mL of 4-NP aqueous solution (0.36 mM) and a certain amount of catalysts were mixed and magnetically stirred for 30 min to ensure the establishment of an adsorption/desorption equilibrium. Then, a certain amount of $H_2O_2$ aqueous solution was added into the reactor. The heterogeneous Fenton-like degradation was carried on during 75 min as soon as the $H_2O_2$ aqueous solution was added. At the intervals of given time, 2 mL of the suspension was collected and the degradation reaction was stopped by adding $n$-butyl alcohol. Then, the suspension was filtered using 0.22 μm membrane filter to remove the catalysts and the 4-NP concentration was determined by using a UV spectrophotometer. The reusability of the catalyst was evaluated by washing and drying the catalyst in air oven at 120 °C for overnight and using it for dye degradation under similar experimental conditions. Each experiment was repeated three times.

## 3. Results and discussion

### 3.1 Thermal stability of Fe-MOF

To prepare magnetic Fe–$C_x$ nanocomposites, the thermal stability of Fe-MOF is important and characterized by TGA in $N_2$ atmosphere at a heating rate of 1 °C min$^{-1}$. The obtained TGA curve, shown in Fig. 1, suggests that it has three steps for mass loss of as-prepared Fe-MOF sample with increasing temperature. The first mass loss is about 3% below 200 °C, which can be attributed to the removal of adsorbed water and DMF. The second mass loss between 200 and 365 °C is 23.2% mainly resulting from the decomposition of oxygen-containing groups in the organic ligands of PTA and DMF of Fe-MOF, and a narrow endothermic peak at 365 °C can be found during the second weight loss process. With the increasing temperature, the mass loss of step 3 from 365 °C to 586 °C may be attributed to the loss of chlorine, the decomposition of aromatic rings, the conformation of iron oxides and the conversion between iron oxides.[34]
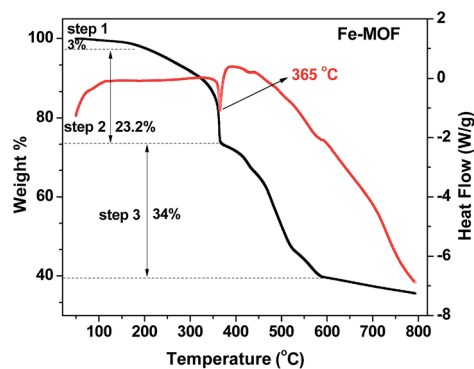
Fig. 1   TGA curves of the as-prepared Fe-MOF from 50 °C to 800 °C.

The conversion could be attributed to the incomplete calcined products as evidenced by thermal stability. After 600 °C, the mass of material was relatively stable. Therefore, the pyrolysis products of Fe-MOF sample from 400 to 600 °C were used as catalyst for the Fenton-like degradation of organic pollution.

The phase of the as-prepared samples under different pyrolysis temperature was demonstrated by powder X-ray diffraction, and depicted in Fig. 2a. From Fig. 2a, we can see six well-defined diffraction peaks at 9.4, 12.6, 16.6, 18.8, 21.9 and 28.4°, which is in accordance with that of MIL-101(Fe) $(Fe_3(O)Cl[C_6H_4(CO_2)_2]_3(C_3H_7NO))$ in previous reported



Fig. 2   (a) Powder XRD patterns and (b) Raman spectra of Fe-MOF and Fe–C$_x$.

literatures.[35,36] After heat treatment at 400 °C, the as-obtained Fe–C$_{400}$ exhibits that the main diffraction peaks appear in three areas between 8 to 10°, 15 to 20° and 28 to 35°, which is different with that of the bare Fe-MOF. It indicates that the phase of Fe-MOF was completely changed at 400 °C because of loss of part of oxygen-containing groups. However, no any diffraction peaks belong to iron oxides, which suggests that the temperature of 400 °C was not enough for the decomposition of the Fe-MOF to iron oxide and carbon, and the Fe–C$_{400}$ was intermediate product between the Fe-MOF and iron oxide/carbon composites. The typical pattern of Fe–C$_{400}$ implies that the Fe–C$_{400}$ may still be metal–organic complexes. When the temperature was increased to 450 °C, part of peaks between 8 and 10° disappear, and new peak raises at $2\theta = 35.5°$, which may be assigned to (311) planes of γ-Fe$_2$O$_3$ (JCPDS no. 39-1346). With the temperature to 500 °C, new diffraction peaks at about 18.6, 30.3, 35.5, 37.3, 43.3, 53.7, 57.2 and 62.7° appear and old diffraction peaks such as 8.2, 9.2, 10, 28 and 35° fall off. The intensity of these new diffraction peaks gradually increases and those pristine diffraction peaks gradually disappear until the temperature was increased to 600 °C. The mainly diffraction peaks of Fe–C$_{600}$, present in Fig. 2a at $2\theta$ values about 18.6, 30.3, 35.4, 37.3, 43.31, 53.7, 57.2 and 62.7° correspond to (111), (220), (311), (222), (400), (422), (511) and (440), respectively, which are readily indexed to a pure phase of Fe$_3$O$_4$ (JCPDS card no. 19-0629). Meanwhile, it indicates that the Fe–C$_x$ (450, 500, 550) are multicomponent.

Fig. 2b shows the Raman spectra of Fe-MOF and Fe–C$_x$. For the Fe-MOF, an apparent characteristic peak at 1612 cm$^{-1}$, as presented in Fig. 2b, is assigned to the vibration of C–C in benzene ring.[37] After heat treatment at 400 °C, we still only observe a characteristic peak at 1599 cm$^{-1}$ for the as-prepared Fe–C$_x$. When the treatment temperature was increased to 450 °C and more, two characteristic peaks at about 1333 cm$^{-1}$ and 1590 cm$^{-1}$ are attributed to the D band (sp$^3$-C) and G band (sp$^2$-C) of carbon, respectively, in addition, the intensity ratio of D band and G band ($I_D/I_G$) increase with the increase of temperature. It indicates that the sp$^2$-C in benzene ring could be decomposed at the temperature up to 450 °C, and the organic ligands of PTA in Fe-MOF were gradually converted to amorphous carbon with the increase of temperature to 600 °C, which are consistent with the XRD results. These amorphous carbon is favour of the dispersion of iron oxides nanoparticles.

SEM image, shown in Fig. 3a, reveals that the Fe-MOF crystals are spindle-like shape with a nonuniform size and smooth surface. After treatment of the Fe-MOF crystals at 400 °C, we can observe that the spindle-like Fe-MOF crystals were transformed into homogeneous Fe–C$_{400}$ particles that are gathered together with single morphology and rough surface (Fig. 3b). When the temperature was increased to 500 °C, it can be seen some graphene-like carbon sheets (Fig. 3c) from the pyrolysis of organic ligands. Moreover, lots of inorganic particles can be observed around these carbon sheets for Fe–C$_{500}$. After the temperature was further increased to 600 °C, the as-prepared Fe–C$_{600}$ (Fig. 3d) exhibit more carbon sheets than that of Fe–C$_{500}$, and many octahedral nanocrystals were formed on the surface of carbon sheets. SEM analyses reveal that different
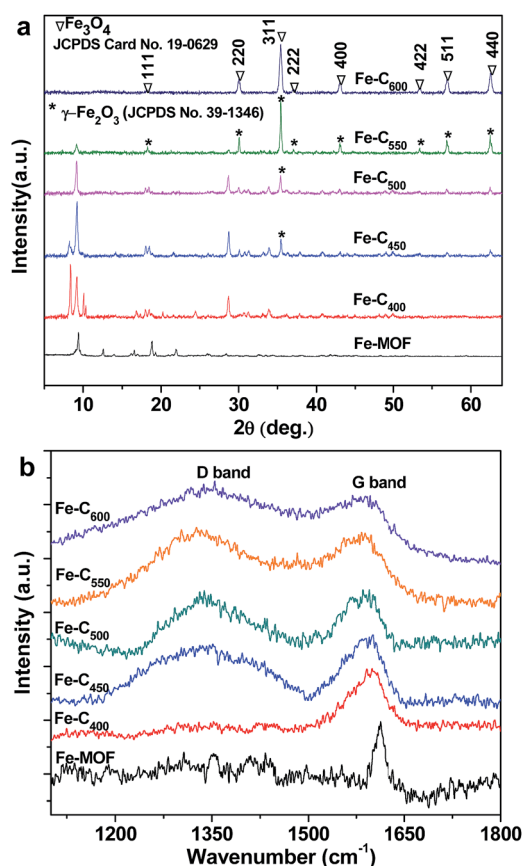
**Fig. 3** SEM images of the (a) Fe-MOF, (b) Fe$-$C$_{400}$, (c) Fe$-$C$_{500}$, and (d) Fe$-$C$_{600}$.

annealing temperatures have a noticeable effect on the morphology of the as-synthesized products.

To study the porosity of all samples, N$_2$ adsorption–desorption isotherms were measured, as depicted in Fig. 4. All of the isotherms present typical type IV profiles and H3 hysteresis loop on the basis of IUPAC classical-cation, indicating the similar pore structures of Fe$-$C$_x$ and the predominance of the mesopore.[38] The H3 hysteresis are typically given by aggregates of plate-shaped particles or adsorbents containing slit-shaped pores,[39,40] implying the presence of carbon sheets in as-prepared Fe$-$C$_x$ samples. Furthermore, the parameters of the porous structure and textural properties are listed in Table S1.† The BET specific surface area of Fe$-$C$_{400}$, Fe$-$C$_{450}$, Fe$-$C$_{500}$, Fe$-$C$_{550}$, Fe$-$C$_{600}$ are 49.1094, 42.9603, 86.6838, 171.2443 and 88.9648 m$^2$ g$^{-1}$ respectively. Besides, the average pore size of these materials is range from 8.3 to 11.8 nm.

Fig. 4b shows the zeta-potential diagrams of Fe$-$C$_x$. The point of zero charge (pH$_{pzc}$) of various Fe$-$C$_x$ ($x$ = 400, 450, 500, 550, 600 °C) was 3.7, 5.9, 4.9, 5.3 and 6.7, respectively. As we known, when pH > pH$_{pzc}$, the surface charge of the materials is negative, and will be positive at pH < pH$_{pzc}$. Therefore, the surface charges of Fe$-$C$_{400}$, Fe$-$C$_{450}$, Fe$-$C$_{500}$, Fe$-$C$_{550}$ were negative in Fenton-like reaction system at circumneutral pH = 6.21, in contrast, the Fe$-$C$_{600}$ was positive.

Fig. 5 show the XPS spectra in the surface of Fe$-$C$_x$ composites. Full-view (Fig. 5a) of XPS spectra indicates that composites have iron, carbon, oxygen, chlorine, and nitrogen elements, which contained in the pristine Fe-MOF (Fe$_3$(O)Cl [C$_6$H$_4$(CO$_2$)$_2$]$_3$(C$_3$H$_7$NO)) (Table S2†). Besides, the gradually decreasing of mass ratios of chlorine and oxygen in the as-prepared Fe$-$C$_x$ composites indicates that the chlorine and oxygen escaped during the production of iron oxides/carbon. Fig. 5b shows the XPS spectra of Fe 2p for Fe-MOF and Fe$-$C$_x$ composites. For the pristine Fe-MOF, we can see two main peaks at 711.5 and 725 eV and a satellite peak at 718.5 eV, which matches well with the MOF of MIL-Fe[41,42] The spectra of Fe 2p for Fe$-$C$_{400}$ and Fe$-$C$_{450}$ show three peaks at 711.5, 715.8 and 724.6 eV, indicating that the chemical environment of Fe(III) had changed but possibly still bonded with benzene rings in as-prepared Fe$-$C$_{400}$ and Fe$-$C$_{450}$. The spectra of Fe 2p for Fe$-$C$_{500}$ and Fe$-$C$_{550}$ show two main peaks at 711.6 and 724.8 eV, and a satellite peak of 718.5 eV, which are in good agreement with the reported values for Fe$_2$O$_3$.[43] It indicates that the most of Fe-MOFs had been converted into iron oxides at the pyrolysis temperature of 500 and 550 °C. For Fe$-$C$_{600}$, the peak positions of Fe 2p$_{3/2}$ and Fe 2p$_{1/2}$ are, respectively, 711.1 and 724.6 eV, and no obviously satellite peak presents, which is well consistent with the results of reported Fe$_3$O$_4$.[43,44] In addition, a peak at 711.1 eV for Fe$-$C$_{550}$ indicates that there have Fe$_3$O$_4$ particles. The C 1s spectra of Fe-MOF and Fe$-$C$_x$ are presented in Fig. 2c. As we can see that the main peak at 284.8 eV for Fe-MOF gradually shifted to 285 eV for Fe$-$C$_{600}$, which confirms the loss of COO groups and pyrolysis of benzene ring. The C 1s spectra of Fe-MOF and Fe$-$C$_x$ can be deconvoluted to three peaks at about 285, 286, and 289.5 eV (Fig. S1†), corresponding to C–C, C–O, and O–C═O groups, respectively. With the increase of temperature, the peak at 289.5 eV gradually disappears (Fig. 5c), indicating that the carbonyl groups were decomposed to CO or CO$_2$ gas gradually. Fig. 5d shows the O 1s
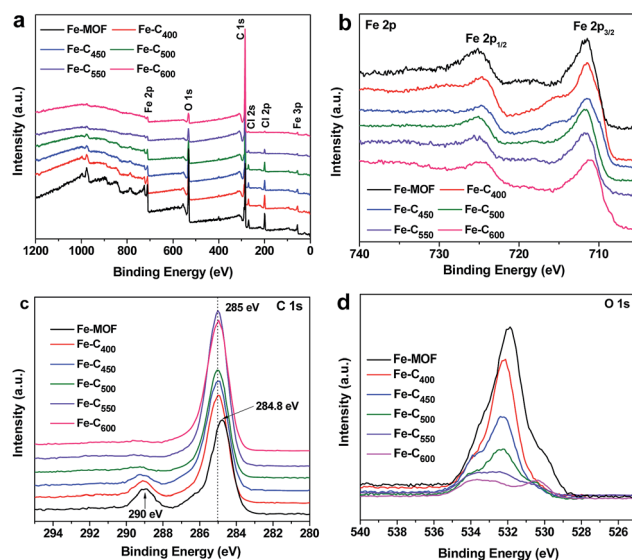


**Fig. 4** (a) Nitrogen adsorption isotherms and (b) zeta-potential curves of Fe$-$C$_x$.



**Fig. 5** XPS spectra of (a) full-view, (b) Fe 2p and (c) C 1s and (d) O 1s for Fe-MOF and Fe$-$C$_x$.

spectra of Fe-MOF and Fe–C$_x$ composites. Obviously, the content of oxygen-containing groups was reduced with the increase of temperature. As shown in Fig. S2a,† the O 1s spectra of Fe-MOF can be fitted to three peaks at 530.1, 531.9 and 533.5 eV, corresponding to Fe–O, C–O, and C=O groups. After heat treatment, all the three peaks shifted to about 530.8, 532.5 and 533.9 eV (Fig. S2†), indicating the change of chemical environment of oxygen in Fe-MOF and Fe–C$_x$. According to the above characterization, the speculated main components of Fe–C$_x$ at different pyrolysis temperature are listed in Table S3.†

## 3.2 Heterogeneous Fenton-like degradation of 4-NP by Fe–C$_x$

**3.2.1 Effect of pyrolysis temperature.** Fig. 6 presents the catalytic efficiencies of pristine Fe-MOF and various Fe–C$_x$ (0.08 g L$^{-1}$) for the heterogeneous Fenton-like degradation of 4-NP (250 mL, 0.36 mM) at unadjusted circumstance pH 6.21 and 18 °C with 7.8 mM of H$_2$O$_2$ dosage. As it shown above, 48.1 wt% 4-NP can be decomposed by pristine Fe-MOF in above catalytic system. Meanwhile, as high as 87.4, 88.0, 89.0, and 83.8 wt% removal efficiency of 4-NP could be achieved within 75 min by using of Fe–C$_{400}$, Fe–C$_{450}$, Fe–C$_{500}$, Fe–C$_{550}$, respectively. However, Fe–C$_{600}$ exhibited weak catalytic activity for the degradation of 4-NP, less than 8 and 4 wt% of 4-NP was degraded, respectively. It indicated that the annealing temperature could significantly affect the Fenton-like catalytic activity of as-prepared Fe–C$_x$, the multicomponent Fe–C$_{500}$ showed the best catalytic activity for the degradation of 4-NP. Furthermore, at the initial of the reaction (30 min), we can observe that the degradation rate of 4-NP on Fe–C$_{450}$ was faster than that of Fe–C$_{500}$ sample, which indicated that the formation rates of Fe$^{2+}$ for the sample of Fe–C$_{450}$ was faster than that of Fe–C$_{500}$ at the beginning of the Fenton-like reaction (Fig. 6).

**3.2.2 Effects of catalyst loading.** To further study the catalytic activity of Fe–C$_{500}$, the influence factors, such as catalyst loading, H$_2$O$_2$ dosage, reaction temperature and initial pH of solution, on the degradation efficiency of 4-NP by Fe–C$_{500}$ were analysed in detail, and shown in Fig. 7. Fig. 7a shows the
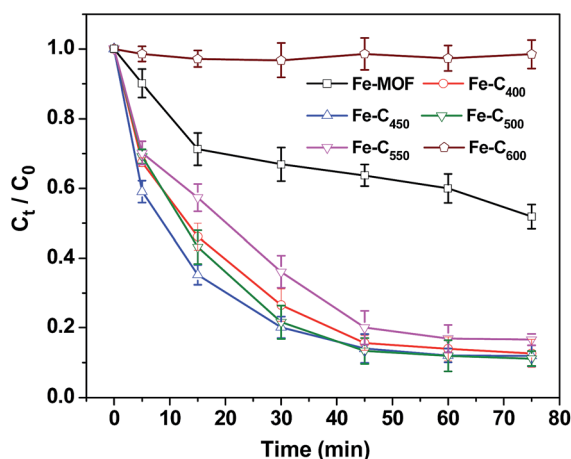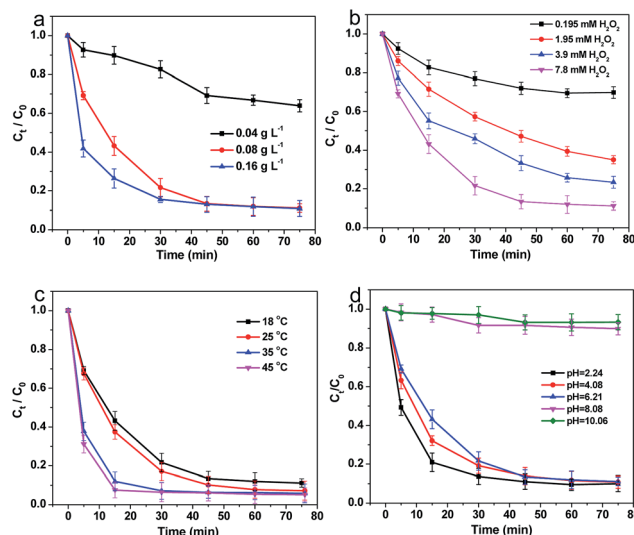


Fig. 7 Effects of reaction conditions on the degradation 4-NP by Fe–C$_{500}$. (a) Catalyst loading, (b) H$_2$O$_2$ dosage, (c) reaction temperature, and (d) initial pH.

degradation of 4-NP using various catalyst loading (0.04, 0.08 and 0.16 g L$^{-1}$) under the aids of 7.8 mM of H$_2$O$_2$ at 18 °C. When the content of Fe–C$_{500}$ was 0.04 g L$^{-1}$, the value of $C_t/C_0$ was high up to be 0.64, while the $C_t/C_0$ can be approached to 0.11 in 75 min with the loading of Fe–C$_{500}$ increasing to 0.08 g L$^{-1}$. In addition, further increasing the concentration of catalysts, the $C_t/C_0$ still stayed near 0.11, but the degradation rate of 4-NP was distinctly accelerated. Therefore, the increase of the catalysts loading was favourable to the degradation of 4-NP in water. To quantitatively evaluate the effect of Fe–C$_{500}$ loading for the catalytic performance, the pseudo-first order equation (eqn (1)) was used to fit the degradation of 4-NP in water.

$$C_t = C_0 \exp(-kt) \tag{1}$$

where $k$ is the apparent rate constant of the 4-NP degradation. The $k$ values were calculated and listed in Table 1. When the loading of catalyst rose from 0.04 to 0.16 g L$^{-1}$, the $k$ value increased from 0.35 to 3.37 h$^{-1}$.

**3.2.3 Effects of H$_2$O$_2$ dosage.** Fig. 7b shows the effects of H$_2$O$_2$ dosage on the removal of 4-NP by 0.08 g L$^{-1}$ catalysts at



Fig. 6 Degradation of 4-NP by Fe-MOF and Fe–C$_x$. [4-NP] = 0.36 mM, catalyst = 0.08 g L$^{-1}$, [H$_2$O$_2$] = 7.8 mM, $T$ = 18 °C, pH 6.21.

Table 1 Pseudo-first order rate constants for 4-NP removal under different conditions using Fe–C$_{500}$ catalysts

| Fe–C$_{500}$ (mg L$^{-1}$) | H$_2$O$_2$ (mM) | $T$ (°C) | $k$ (h$^{-1}$) | $R$ |
|---|---|---|---|---|
| 0.04 | 7.8 | 18 | 0.35 | 0.90948 |
| 0.08 | 7.8 | 18 | 2.98 | 0.98997 |
| 0.16 | 7.8 | 18 | 3.37 | 0.81872 |
| 0.08 | 7.8 | 25 | 3.48 | 0.99255 |
| 0.08 | 7.8 | 35 | 8.29 | 0.95969 |
| 0.08 | 7.8 | 45 | 10.1 | 0.96416 |
| 0.08 | 0.195 | 18 | 0.35 | 0.90013 |
| 0.08 | 1.95 | 18 | 0.83 | 0.97503 |
| 0.08 | 3.9 | 18 | 1.28 | 0.96035 |

18 °C. Obviously, the higher dosage of $H_2O_2$ could result in the higher degradation efficiency as $C_t/C_0$ almost reached 0.11 in 60 min using 7.8 mM of $H_2O_2$. When the concentration of $H_2O_2$ was increased from 0.195 mM to 7.8 mM, $k$ rose from 0.35 to 2.99 $h^{-1}$. Overall, $H_2O_2$ dosage played an important role in degradation of 4-NP, and a sufficient $H_2O_2$ dosage was needful for effectively removal of pollutants.

**3.2.4 Effects of reaction temperature.** The effect of reaction temperature was studied by changing the temperature of 4-NP solution from 18 °C to 45 °C. When the temperature was increased from 18 °C to 35 °C, the kinetics became much faster from $k$ of 3.37 $h^{-1}$ to $k$ of 8.29 $h^{-1}$ (Fig. 7c), which demonstrated the higher temperature could enhance the degradation of 4-NP. Similarly, the $k$ increased to 10.1 $h^{-1}$ with the temperature up to 45 °C.

As the $k$ value increased at higher temperatures, the Arrhenius equation was adopted to calculate the activation energy as the following equation:

$$\ln k = \ln k_0 - \frac{E_a}{R}\frac{1}{T} \qquad (2)$$

where $E_a$ represents the activation energy (kJ $mol^{-1}$), $k_0$ means the temperature-independent factor (g $mg^{-1}$ $min^{-1}$); $T$ denotes the solution temperature in Kelvin (K) and $R$ is the universal gas constant. The Arrhenius linear plot of the degradation of 4-NP by Fe–C$_{500}$ (0.08 g $L^{-1}$) with the addition of 7.8 mM $H_2O_2$ at four different temperature is presented in Fig. S3.† The $E_a$ of the reaction on the Fe–C$_{500}$ surface evaluated by plotting $\ln k$ against $1/T$ and was 38.5 kJ $mol^{-1}$. This value is higher than the activation energy of the diffusion-controlled reactions, which usually ranges in 10–13 kJ $mol^{-1}$.[45] It indicates that the Fenton reaction rate is dominated by the rate of intrinsic chemical reactions on the Fe–C$_{500}$ surface rather than the rate of mass transfer. The value of $E_a$ in our study is between 20.7 and 56.1 kJ $mol^{-1}$ of the activation energy of Fenton reactions using different heterogeneous catalysts from literature data,[46] indicating that Fe–C$_{500}$ composite showed a high catalytic activity in heterogeneous Fenton reaction of 4-NP.

**3.2.5 Effects of initial pH.** The effect of pH (Fig. 7d) was also investigated by changing the initial pH of 4-NP solvents to 2.24, 4.08, unadjusted 6.21, 8.08 and 10.06, corresponding to acidic, circumneutral and basic conditions, respectively. The degradation rate of 4-NP was faster at initial pH = 2.24 and 4.08, which suggested that the acid condition is beneficial to the catalytic degradation. In addition, the degradation of 4-NP was efficient without adjusting the initial pH (6.21) of reaction solution. When the initial pH of solution was adjusted to 8.08 and 10.06, the 4-NP removal by oxidation scarcely occurred.

### 3.3 Recyclability of Fe–C$_{500}$

The potential to reuse Fe–C$_{500}$ for degradation of 4-NP was tested and shown in Fig. 8a. At the 1st cycle, 89.0 wt% of 4-NP can be degraded, and reduced to 61.1 wt% at the 2nd cycle. It is mainly attributed to that part of iron in Fe–C$_{500}$ was dissolved during the 1st cycle. After two cycles, the Fenton-like catalytic activity of Fe–C$_{500}$ was stable, 54.2 and 52.4 wt% 4-NP was
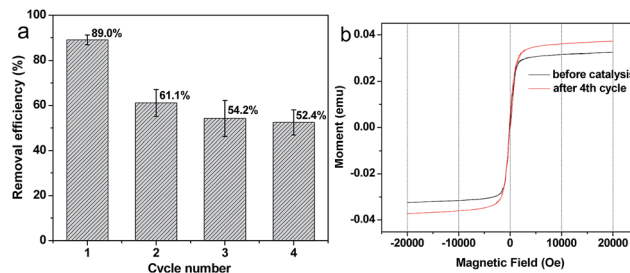


**Fig. 8** (a) Reusable degradation activity for Fe–C$_{500}$ up to 4 cycles and (b) hysteresis loop of Fe–C$_{500}$ before catalysis and after 4 cycles.

removed at the 3rd and 4th cycle, respectively. Fig. 8b shows the hysteresis loop of Fe–C$_{500}$ before catalysis and after 4 cycles. A typical "S"-like shape of the hysteresis loop was observed, indicating the paramagnetic properties of the samples, and the magnetic Fe–C$_{500}$ can be easily recovered by using a magnet after 4 cycles (Fig. S4†). In addition, the saturation magnetization of Fe–C$_{500}$ after 4 cycles is higher than that of the catalyst before the catalytic reaction, which imply that the loss of iron from Fe–C$_{500}$ mainly come from the iron-organic ligands but not the iron oxides.

## 4. Conclusions

In summary, various Fe–C$_x$ nanocomposites could be prepared using Fe-MOF as precursors under $N_2$ protection. The pyrolysis temperature could affect the component, structure and morphology of as-prepared Fe–C$_x$ nanocomposites. Furthermore, the reaction condition, such as the catalyst loading, $H_2O_2$ dosage, reaction temperature, and initial pH could significantly affect the catalytic degradation of 4-NP on the surface of Fe–C$_x$ nanocomposites. The oxidation degradation of 4-NP indicated that the Fe–C$_{500}$ showed the best heterogeneous Fenton-like catalytic activity with 89.0 wt% removal efficiency of 250 mL 0.36 mM of 4-NP within 75 min by using 0.08 g $L^{-1}$ of catalyst loading and 7.8 mM $H_2O_2$ at 18 °C. Furthermore, the magnetic Fe–C$_{500}$ can be easily recycled by using a magnet. The impressive results showed that the preparation of magnetic carbon nanocomposites derived from Fe-MOFs at suitable pyrolysis temperature is an effective route to fabricate high performance Fenton-like catalyst for degradation of organic pollutants in aqueous solution.

## Conflicts of interest

There are no conflicts to declare.

## Acknowledgements

# Notes and references

1 A. Myridakis, G. Chalkiadaki, M. Fotou, M. Kogevinas, L. Chatzi and E. G. Stephanou, *Environ. Sci. Technol.*, 2016, **50**, 932–941.

2 Y. Z. Gong, K. Baylis, R. Kozak and G. Bull, *Agr. Econ.*, 2016, **47**, 411–421.

3 F. Zietzschmann, C. Stuetzer and M. Jekel, *Water Res.*, 2016, **92**, 180–187.

4 S. Y. Jia, Z. Yang, W. B. Yang, T. T. Zhang, S. P. Zhang, X. Z. Yang, Y. Y. Dong, J. Q. Wu and Y. P. Wang, *Chem. Eng. J.*, 2016, **283**, 495–503.

5 J. Li, R. Kang, X. Tang, H. She, Y. Yang and F. Zha, *Nanoscale*, 2016, **8**, 7638–7645.

6 T. T. More, J. S. Yadav, S. Yan, R. D. Tyagi and R. Y. Surampalli, *J. Environ. Manage.*, 2014, **144**, 1–25.

7 O. G. Apul and T. Karanfil, *Water Res.*, 2015, **68**, 34–55.

8 S. Hokkanen, A. Bhatnagar and M. Sillanpaa, *Water Res.*, 2016, **91**, 156–173.

9 D. Chen, W. Shen, S. Wu, C. Chen, X. Luo and L. Guo, *Nanoscale*, 2016, **8**, 172–179.

10 S. Giannakis, F. A. G. Vives, D. Grandjean, A. Magnet, L. F. De Alencastro and C. Pulgarin, *Water Res.*, 2015, **84**, 295–306.

11 S. G. Ardo, S. Nelieu, G. Ona-Nguema, G. Delarue, J. Brest, E. Pironin and G. Morin, *Environ. Sci. Technol.*, 2015, **49**, 4506–4514.

12 X. Li, Z. Wang, B. Zhang, A. I. Rykov, M. A. Ahmed and J. Wang, *Appl. Catal., B*, 2016, **181**, 788–799.

13 S. H. Yoo, D. Jang, H.-I. Joh and S. Lee, *J. Mater. Chem. A*, 2017, **5**, 748–755.

14 Y. Yao, H. Chen, J. Qin, G. Wu, C. Lian, J. Zhang and S. Wang, *Water Res.*, 2016, **101**, 281–291.

15 M. Munoz, Z. M. de Pedro, J. A. Casas and J. J. Rodriguez, *Appl. Catal., B*, 2015, **176–177**, 249–265.

16 H. Lv, H. Zhao, T. Cao, L. Qian, Y. Wang and G. Zhao, *J. Mol. Catal. A: Chem.*, 2015, **400**, 81–89.

17 K.-Y. A. Lin and F.-K. Hsu, *RSC Adv.*, 2015, **5**, 50790–50800.

18 X.-J. Yang, X.-m. Xu, J. Xu and Y.-F. Han, *J. Am. Chem. Soc.*, 2013, **135**, 16058–16061.

19 H. Chen, Z. L. Zhang, Z. L. Yang, Q. Yang, B. Li and Z. Y. Bai, *Chem. Eng. J.*, 2015, **273**, 481–489.

20 J. H. Deng, J. Y. Jiang, Y. Y. Zhang, X. P. Lin, C. M. Du and Y. Xiong, *Appl. Catal., B*, 2008, **84**, 468–473.

21 I. S. X. Pinto, P. Pacheco, J. V. Coelho, E. Lorencon, J. D. Ardisson, J. D. Fabris, P. P. de Souza, K. W. H. Krambrock, L. C. A. Oliveira and M. C. Pereira, *Appl. Catal., B*, 2012, **119**, 175–182.

22 L. Xu and J. Wang, *Appl. Catal., B*, 2012, **123–124**, 117–126.

23 M. J. Jin, M. C. Long, H. R. Su, Y. Pan, Q. Z. Zhang, J. Wang, B. X. Zhou and Y. W. Zhang, *Environ. Sci. Pollut. Res.*, 2017, **24**, 1926–1937.

24 Y. Pan, M. Zhou, X. Li, L. Xu, Z. Tang and M. Liu, *Sep. Purif. Technol.*, 2016, **169**, 83–92.

25 L. Yu, X. Yang, Y. Ye and D. Wang, *RSC Adv.*, 2015, **5**, 46059–46066.

26 V. Cleveland, J.-P. Bingham and E. Kan, *Sep. Purif. Technol.*, 2014, **133**, 388–395.

27 M. Goncalves, M. C. Guerreiro, L. C. de Oliveira and C. S. de Castro, *J. Environ. Manage.*, 2013, **127**, 206–211.

28 M. R. Carrasco-Diaz, E. Castillejos-Lopez, A. Cerpa-Naranjo and M. L. Rojas-Cervantes, *Microporous Mesoporous Mater.*, 2017, **237**, 282–293.

29 Y. Yao, H. Chen, C. Lian, F. Wei, D. Zhang, G. Wu, B. Chen and S. Wang, *J. Hazard. Mater.*, 2016, **314**, 129–139.

30 C. Zhang, F. Ye, S. Shen, Y. Xiong, L. Su and S. Zhao, *RSC Adv.*, 2015, **5**, 8228.

31 X. Li, A. I. Rykov, B. Zhang, Y. Zhang and J. Wang, *Catal. Sci. Technol.*, 2016, **6**, 7486–7494.

32 K. A. Lin and B. J. Chen, *Chemosphere*, 2017, **166**, 146–156.

33 X. Cao, B. Zheng, X. Rui, W. Shi, Q. Yan and H. Zhang, *Angew. Chem., Int. Ed.*, 2013, DOI: 10.1002/anie.201308013.

34 L. Wang, Y. Zhang, X. Li, Y. Xie, J. He, J. Yu and Y. Song, *Sci. Rep.*, 2015, **5**, 14341.

35 X. Cai, J. Lin and M. Pang, *Cryst. Growth Des.*, 2016, **16**, 3565–3568.

36 T. Yamada, K. Shiraishi, H. Kitagawa and N. Kimizuka, *Chem. Commun.*, 2017, **53**, 8215–8218.

37 G.-T. Vuong, M.-H. Pham and T.-O. Do, *CrystEngComm*, 2013, **15**, 9694.

38 Y. Li, Q. Zhang, J. Zhang, L. Jin, X. Zhao and T. Xu, *Sci. Rep.*, 2015, **5**, 14155.

39 K. S. W. Sing and R. T. Williams, *Adsorpt. Sci. Technol.*, 2004, **22**, 773–782.

40 M. Díaz Ramos, G. I. Giraldo Gómez and N. Sanabria González, *J. Mol. Catal. B: Enzym.*, 2014, **99**, 79–84.

41 S.-H. Huo and X.-P. Yan, *J. Mater. Chem.*, 2012, **22**, 7449.

42 W. Cho, S. Park and M. Oh, *Chem. Commun.*, 2011, **47**, 4138–4140.

43 T. Yamashita and P. Hayes, *Appl. Surf. Sci.*, 2008, **254**, 2441–2449.

44 J. A. Cuenca, K. Bugler, S. Taylor, D. Morgan, P. Williams, J. Bauer and A. Porch, *J. Phys.: Condens. Matter*, 2016, **28**, 106002.

45 S.-S. Lin and M. D. Gurol, *Environ. Sci. Technol.*, 1998, **32**, 1417–1423.

46 L. Xu and J. Wang, *Environ. Sci. Technol.*, 2012, **46**, 10145–10153.